Research Square

Preprints are preliminary reports that have not undergone peer review.
They should not be considered conclusive, used to inform clinical practice,
or referenced by the media as validated information.

Differential Photoacoustic CO 2 Gas Detection with Two Commercial MEMS Microphones

Mengyuan Wang
Harbin Institute of Technolog
Penghong Shi
Harbin Institute of Technolog
Jiaqi Chang
Instrumentation Technology and Economy Institute
Minjie Zhu
Instrumentation Technology and Economy Institute
Bing Li
Harbin Institute of Technolog
Gaopeng Xue
xuegaopeng@hit.edu.cn
Harbin Institute of Technolog

Research Article

Keywords: Photoacoustic spectroscopy, gas detection, differential photoacoustic cell, MEMS microphones

Posted Date: October 8th, 2026

DOI: https://doi.org/10.21203/rs.3.rs-11099049/v1

License: This work is licensed under a Creative Commons Attribution 4.0 International License.
Read Full License

Additional Declarations: No competing interests reported.

Abstract

A differential photoacoustic spectroscopy (PAS) platform for CO_2 quantification is reported. The system employs a differential photoacoustic cell (PAC) and two commercial MEMS microphones. The PAC is constructed from a pair of matched longitudinal acoustic channels connected through common buffer volumes. This layout produces antiphase pressure oscillations with balanced magnitudes, so that differential readout reinforces the resonant signal while suppressing common-mode disturbance. The fabricated cell exhibited a first-order resonance at 5260 Hz with a quality factor of 36. Under wavelength modulation, the differential PAS system maintained linear behavior across a CO_2 concentration range of 1000–50000 ppm, with a coefficient of determination R^2 of 0.993. In the lower range of 1000–10000 ppm, the linearity improved further to R^2 = 0.999, and the calibration slope was approximately 0.0055 μV/ppm. Relative to a conventional single-channel PAC, the differential architecture provided about a twofold signal gain and better linearity. Allan–Werle analysis gave a detection limit of 14.3 ppm at an integration time of 100 s. The differential detection scheme therefore offers a compact and sensitive route to trace gas sensing with effective noise rejection.

1 Introduction

Quantitative analysis of trace gases is important in atmospheric monitoring (Wokosin et al. 2026), industrial safety (Albatayneh et al. 2025), and noninvasive breath-based diagnosis (Li et al. 2025). Real-time identification of hazardous or dilute atmospheric species is particularly valuable for reducing workplace exposure and enabling early pathological screening (Wang et al. 2026). Over the past decade, many sensing platforms have matured for gas recognition, including potentiometric electrochemical transducers (Fendrych et al. 2025, Huang et al. 2023), semiconducting metal-oxide films (Qian et al. 2024, Gu et al. 2026, Naricetti et al. 2026), piezoelectric acoustic-wave devices (Kilic et al. 2025, Kumar et al. 2026), and optical analytical methods (Qian et al. 2025, Fard et al. 2025, Cavallaro et al. 2026). Among optical techniques for dilute species, tunable diode laser absorption spectroscopy (TDLAS) provides strong selectivity through spectral fingerprinting, but its sensitivity is constrained by the optical path length, which complicates miniaturization (Peng et al. 2026, Yang et al. 2026). PAS, in contrast, relies on the photoacoustic effect, in which absorbed optical energy is converted into a detectable pressure wave (Zhang et al. 2026, Chen et al. 2026). In PAS, intensity-modulated light first populates excited states of the target molecules. Subsequent radiationless de-excitation converts part of the absorbed energy into transient local heating. When the excitation is periodic, this heating launches an acoustic wave at the modulation frequency, which can be sensed by an acoustic transducer (Mu et al. 2026, Zhang et al. 2025). PAS therefore combines strong selectivity, high sensitivity, and intrinsic zero-background detection.

For a PAS instrument, the achievable signal-to-noise ratio (SNR) and the lowest measurable concentration are largely determined by the acoustic detection element. Acoustic receivers can be broadly divided into resonant and non-resonant types. Resonant approaches, especially cantilever-enhanced photoacoustic spectroscopy (CEPAS) and quartz-enhanced photoacoustic spectroscopy

(QEPAS), have been developed as alternatives to conventional electroacoustic transducers. Although quartz tuning forks used in QEPAS offer very high quality factors (*Q*), they require stringent optical alignment within the confined spacing between the prongs, which complicates assembly and reduces mechanical robustness (Lang et al. 2022, Sang et al. 2025). In CEPAS, cantilever displacement is interrogated by optical interferometry. This leads to penalties in footprint and system complexity, limiting further miniaturization (Yang et al. 2025a, Yan et al. 2025). Silicon-based MEMS resonators using capacitive (Trzpil et al. 2022, Yin et al. 2024) or piezoresistive (Liu et al. 2026, Xue et al. 2026) transduction exploit well-defined mechanical resonances, offering improved sensitivity, sharp frequency selectivity, and natural structural miniaturization. By contrast, non-resonant options such as thin-film capacitive microphones have simple structures, good transient response, and broadband frequency coverage (Jiang et al. 2026, Chen et al. 2025). However, their sensitivity does not benefit from frequency-selective amplification and is ultimately limited by thermal noise floors, so the resonant gain available to resonant devices cannot be exploited.

Differential PAS has emerged as another route to improved performance and has attracted considerable interest for background suppression and sensitivity enhancement. To increase detection sensitivity, a photoacoustic cell (PAC) may also be incorporated so that the generated PA pressure is amplified. In a differential PAC, two geometrically matched resonant chambers are connected to buffer zones; the two acoustic channels then produce pressure disturbances that are equal in magnitude but opposite in phase (Yang et al. 2025b). Acoustic receivers placed at the longitudinal center of each resonator capture the corresponding photoacoustic signals. Differential amplification then cancels common-mode interference while retaining the antiphase signal components. The resulting signal is enhanced in two ways: constructive combination of the antiphase photoacoustic responses and resonant amplification provided by the cell geometry. This leads to a marked SNR improvement and a lower minimum detectable concentration. For example, a differential quartz-enhanced photoacoustic spectroscopy (D-QEPAS) sensor based on a differential PAC has been reported; its second harmonic (2*f*) signal amplitude was 1.65 times that of a single quartz tuning fork (Zhang et al. 2023).

To reduce background noise and improve the detection SNR, this work introduces a differential PAS gas measurement system that employs a differential PAC together with two commercial MEMS microphones. To improve noise rejection and detection SNR, this work develops a differential PAS system that combines a paired-resonator PAC with two commercial MEMS microphones. The design exploits both the antisymmetric acoustic response of the cell and the resonant gain of the longitudinal channels. The spectral and acoustic behavior of the cell is examined theoretically and experimentally. The system is then evaluated for CO_2 detection over a wide dynamic range, and its long-term stability is assessed by Allan–Werle analysis. The spectral and acoustic responses of the differential PAC are examined through theoretical analysis and experimental verification, respectively. Finally, the constructed differential PAS gas measurement system was found to provide good linearity over a wide dynamic range of CO_2 concentration. An Allan–Werle deviation analysis was also carried out to quantify the system's long-term stability.

2 Differential PAS gas measurement system

2.1 Concept of differential PAS gas measurement system

Figure 1 shows the schematic of the differential PAS gas measurement system. The main parts are a differential PAC, two MEMS microphones, and a laser power source. The PAC is configured as a pair of acoustically matched longitudinal resonators connected through common buffer volumes. Gas enters through the buffer region on one side and leaves through the buffer region on the other. A target gas (CO_2) at a given concentration is introduced into the PAC. The buffer volumes help suppress flow-related noise. When a modulated laser beam passes through one of the acoustic channels, the resonant acoustic field established in that channel is coupled through the buffer region into the second channel, which acts as the reference channel. Because the two channels support the same longitudinal mode, their pressure oscillations are antiphase with nearly balanced magnitudes. Under the first-order longitudinal standing-wave mode, the gas in the two channels undergoes periodic compression and expansion in opposite directions. Thus, although optical energy is introduced into only one channel, acoustic coupling through the buffer volumes allows out-of-phase pressure disturbances to be detected in the reference channel. Two acoustic sensors, for example MEMS microphones, serve as the acoustic transducers. When the detected signals are differentially processed, both resonant signal enhancement and noise suppression can be achieved simultaneously.

2.2 Design and simulation of a differential PAC for PAS measurement system

The cell geometry was selected so that the first longitudinal resonance lies within the 5000–6000 Hz band, where ambient acoustic noise is relatively low and the MEMS microphones used in this work operate efficiently. For a straight cylindrical resonator with rigid ends, the first longitudinal mode is mainly governed by the channel length. If the channel is approximated as an ideal pipe, the resonance condition is $f = c / 2L_1$ where f is the resonant frequency, c is the speed of sound, and L_1 is the geometric channel length. In the present design, however, the two ends of each channel are connected to buffer volumes rather than being perfectly closed. These buffer regions isolate flow noise and stray acoustic disturbances, but they also perturb the effective acoustic length. A standard end-correction term was therefore introduced, giving $L_{eff} = L_1 + 1.2R$ and a corrected first-order resonance of $f = c / (2(1.2R_1 + L_1))$. Using this relation, the channel length and diameter were set to $L_1 = 29.2$ mm and $R_1 = 3$ mm, while the buffer zones were assigned $L_2 = 20.4$ mm and $R_2 = 15$ mm, respectively. These dimensions place the calculated first-order resonance at 5222 Hz.

A three-dimensional thermoviscous acoustic model was then used to examine how the real cell geometry, including the buffer volumes and the pressure-extraction holes, modifies the idealized prediction. Optical absorption was represented by a volumetric heat source of 1 W/m³ applied to one channel. The simulated pressure field, shown in Fig. 2(b), gives a first-order resonance at 5164.1 Hz. The

difference from the analytical estimate is only 1.1%, which indicates that the end-corrected pipe model captures the dominant acoustic behavior of the cell. The simulation also shows that the two channels support pressure oscillations of nearly equal magnitude but opposite sign, as required for differential detection. Since the microphone response is strongest at the pressure antinodes, the microphones were placed at those locations. To avoid disturbing the acoustically rigid boundary, pressure was extracted through 1 mm micro-holes rather than by direct mounting. These holes preserve the longitudinal mode and transfer the pressure signal to the microphones with minimal perturbation. In the color map, blue to red represents increasing acoustic pressure amplitude, while green indicates zero acoustic pressure. The simulated field shows an antisymmetric pressure distribution between the two channels, which is consistent with the intended differential operation. Based on this acoustic pressure distribution, optimal response sensitivity requires the MEMS microphones to be placed at the pressure antinodes, where the pressure is maximum. An indirect pickup scheme is adopted to prevent disturbance of the acoustically rigid boundary and avoid leakage. In this scheme, micro-holes of 1 mm diameter at the pressure antinodes of the channel act as pressure extraction ports. Such micro-holes maintain the acoustic mode and transfer pressure efficiently to the MEMS microphones, which allows photoacoustic sensing with high fidelity and low perturbation.

3 Experimental results

3.1 Measurement setup of the differential PAS system

The measurement setup shown in Fig. 3 was constructed to evaluate the performance of the differential PAS system: (a) schematic diagram and (b) actual setup. The inner surfaces of the PAC's acoustic resonant channels were polished to reduce viscous damping, while the gas inlet and outlet were positioned in the buffer zones at the ends. On both sides of the PAC, two calcium fluoride (CaF_2) windows with a diameter of 25 mm were installed. After collimation by a fiber collimator, the laser beam was directed along the axial centerline of the acoustic resonant channel without obstruction. The beam spot was centered on the channel axis by adjusting a five-axis alignment stage, which prevented wall-scattering noise caused by beam clipping. At the output end, the transmitted power was monitored with an optical power meter so that the excitation power remained constant during the experiment. The excitation source was a 2004 nm (4990 cm^{-1}) distributed feedback (DFB) diode laser (Shenzhen Netopto Technology, EP2004-0-DM-DX1-FM) with 1.5 mW output power; its wavelength coincides with a strong near-infrared CO_2 absorption peak. Various CO_2 concentrations were generated at controlled flow rates by mixing 10% CO_2 gas (balanced with N_2) and pure N_2 in a gas mixer (GRLH, GR-7050).

A commercial integrated circuit board (MF168) combines a function generator and a lock-in amplifier in one module, which simplifies modulation of the infrared source. This board simultaneously provides a high-frequency sinusoidal wave for laser wavelength modulation and a low-frequency sawtooth wave for slow periodic scanning. By superposing the two signals, the DFB laser is driven so that its instantaneous wavelength sweeps across the whole absorption line of the target gas, thereby allowing the full

absorption spectrum to be acquired in the time domain. A 600 mV bias was applied across the MEMS microphones in order to prevent reverse-breakdown damage. Laser-induced acoustic signals in the gas were converted into electrical signals by the two MEMS microphones; these signals were then differentially subtracted and sent to the MF168. The built-in lock-in amplifier demodulated the signals at the first harmonic (1*f*), and the output was then sent to a computer and displayed through host software. In addition, the selectivity of PAS makes it possible to avoid interference from complex gas mixtures effectively. The DFB laser includes temperature control to ensure stable wavelength locking and output, and the gas mixer offers a stable background for dynamic mixing; these features enable high-precision calibration. Taken together, these measures ensure that the overall system has excellent detection stability.

3.2 Resonant characteristic and acoustic response of the fabricated differential PAC

The differential PAC is another core component of PA measurement systems for trace gas detection, and its resonant frequency and quality factor (*Q* factor) are key parameters. Over the measurement band, the MEMS microphones exhibit a flat response, so variations in signal amplitude reflect only the acoustic characteristics of the differential PAC. At a fixed gas concentration, the excitation frequency was swept from 5100 to 5400 Hz by wavelength modulation spectroscopy, and the PA signal amplitudes were recorded. To obtain the actual frequency response of the differential PAC, the measured amplitudes were fitted with a Lorentzian curve, as shown in Fig. 4. From the fit, the first-order resonant frequency (f_c) was determined to be 5260 Hz, which is close to the simulated 5164.1 Hz. The *Q* factor was calculated to be 36, meaning that the generated acoustic wave could be amplified to enhance trace gas detection.

The differential performance of the differential PAC was characterized by analyzing the output differential 1*f* PA signals from the two microphones at a modulation period of 10 s for a given CO_2 concentration, as shown in Fig. 5. The two microphones produced signals of similar magnitude but opposite polarity. The phase difference was close to 180°, in agreement with the simulated field distribution in Fig. 2(b). This confirms that the fabricated cell supports the intended antisymmetric mode. The slight amplitude imbalance between the two channels is attributed to machining and assembly tolerances, and it can be compensated during differential processing. After subtraction, the effective amplitude was approximately the sum of the individual channel amplitudes, which is consistent with the expected differential gain.

3.3 Gas detection

CO_2 measurements were carried out with the constructed detection system using 1*f* wavelength modulation spectroscopy in order to assess the performance improvement of the differential PAC. Through the host computer, the MF168 was set to produce a 0.1 Hz, 0.4–1.0 V sawtooth for slow wavelength sweeping, on which a 5260 Hz, 100 mV sine wave was superimposed for high-frequency

modulation. The lock-in time constant was 100 ms. Various CO_2 gas samples were prepared by mixing pure N_2 with a 10% CO_2 standard gas at preset ratios, after which they were injected into the PAC. The DFB laser was driven by the modulated output of the MF168; its beam entered the cell and excited acoustic signals through the photoacoustic effect. The acoustic signals were captured by the MEMS microphones so that the absorption spectra could be recorded. 1*f* PA signals at a modulation period (4 s) were recorded at different CO_2 gas concentrations in a wide concentration range of 1000–50000 ppm, as shown in Fig. 6(a). When the gas concentration was reduced from 50000 ppm to 45000, 40000, 35000, 30000, 25000, 20000, 15000, 10000, 7000, 4000, and 1000 ppm, the PA signal amplitudes decreased accordingly from 275 to 4.5 μV. Figure 6(b) presents the relationship between the 1*f* signal peak values and CO_2 gas concentrations. The linear fit gave a determination coefficient R^2 of 0.993, which indicates that the system has a good linearity to gas concentrations over a wide range. It is notable that in the low concentration range of 1000–10000 ppm, the determination coefficient R^2 reached 0.999, showing a more precise linear response. For this differential PA system, the sensitivity was estimated to be about 0.0055 μV/ppm. With pure N_2 filling the PAC, the background noise standard deviation was calculated to be about 0.548 μV. Based on the 3σ criterion, the system's minimum detection limit was calculated to be about 304 ppm.

Comparative experiments were performed with a single-channel PAC under identical conditions in order to highlight the performance differences between the differential PAC and the conventional single-channel PAC. Figure 7(a) shows the recorded 1*f* PA signals at a modulation period (4 s) at different CO_2 gas concentrations in a wide concentration range of 1000–50000 ppm. When the gas concentration was lowered from 50000 ppm to 45000, 40000, 35000, 30000, 25000, 20000, 15000, 10000, 7000, 4000, and 1000 ppm, the PA spectrum signal amplitudes decreased accordingly from 136 μV to 4.25 μV. Figure 7(b) presents the relationship between the 1*f* signal peak values and CO_2 gas concentrations; linear fitting gave a determination coefficient R^2 of 0.981. For this PA system, the sensitivity was estimated to be about 0.0027 μV/ppm. The signal amplitude from the differential cell was approximately double that from the single-channel cell. It also agreed better with the theoretical linear relationship between signal amplitude and gas concentration. These results indicate that the differential configuration provides notable advantages in both signal enhancement and linear response fidelity.

3.4 Allan-Werle deviation

The sensitivity and long-term stability of the differential PAS measurement system was evaluated by analyzing the Allan-Werle deviation. The differential PAC was flushed with pure N_2 for more than 30 min, and the 1*f* signal time series was recorded during this period. Figure 8 shows the Allan-Werle deviation result by utilizing pure N_2. At first, it increases during the initial 1 s of integration time. Such anomalous behavior is caused by the signal-processing chain at short integration time. After that, it decreased from 2 to 120 s and then leveled off at 120 s. Figure 8 indicates that the detection limit of the differential PAS measurement system reached 14.3 ppm when the integration time was 100 s. The normalized noise equivalent absorption (NNEA) coefficient *N* is introduced to standardly compare with other PA gas

sensors. The NNEA value of this system was calculated as 2.1×10^{-8} W·cm^{-1}·Hz$^{-1/2}$ by using $N = \alpha_{min} \cdot P \cdot t^{1/2}$ (Xue et al. 2026), where P = 1.5 mW is the laser power, t = 100 s is the integration time, and $\alpha_{min} = 1.4 \times 10^{-6}$ cm^{-1} is the minimum detectable absorption coefficient. The minimum detectable absorption coefficient is expressed as $\alpha_{min} = S \cdot N \cdot C$, in which $S = 3.97 \times 10^{-21}$ cm^2·molecule^{-1} is the line strength of the CO_2 transition at 2004 nm, $N = 2.46 \times 10^{19}$ molecule·cm^{-3} is the molecular number density at 296 K and 1 atm, and C = 14.3 ppm is the experimental detection limit, respectively.

4 Conclusion

This work has demonstrated a differential photoacoustic spectroscopy gas measurement system for CO_2 detection. The system combines a paired-resonator photoacoustic cell with two commercial MEMS microphones. The cell uses two longitudinal acoustic channels connected through common buffer volumes. This layout supports an antisymmetric acoustic response, so that differential readout enhances the resonant signal while rejecting in-phase disturbance. Theoretical analysis based on the Helmholtz equation with acoustic end-correction gave a first-order resonant frequency of 5222 Hz. Numerical simulation with a thermoviscous acoustic formulation gave a resonant frequency of 5164.1 Hz, corresponding to a deviation of only 1.1%. For the fabricated cell, the measured first-order resonance was 5260 Hz with a Q factor of 36, indicating effective resonant amplification for trace gas detection. The two microphones produced antiphase signals with comparable magnitudes, which is consistent with the simulated antisymmetric field distribution. Differential subtraction approximately doubled the effective amplitude relative to a single channel. The differential PAS system showed a good linearity for CO_2 detection over 1000–50000 ppm, with a coefficient of determination R^2 of 0.993. In the lower range of 1000–10000 ppm, the linearity improved to R^2 = 0.999, and the calibration slope was about 0.0055 μV/ppm. Using 3σ criterion, the minimum detectable concentration was estimated to be about 304 ppm. Compared with a conventional single-channel cell under the same experimental conditions, the differential configuration provided roughly a twofold signal gain and better linearity (0.993 versus 0.981). Allan-Werle analysis indicated long-term stability and gave a detection limit of 14.3 ppm at an integration time of 100 s. The corresponding NNEA coefficient was estimated as 2.1×10^{-8} W·cm^{-1}·Hz$^{-1/2}$ for standardized comparison. Future studies will aim to optimize the structural design of the differential PAC for higher resonant gain, improve the differential signal processing algorithm to compensate better for channel asymmetry, and enhance overall system integration.

Declarations

Conflict of interest

The authors declare no competing interests.

Author Contribution

M.W. contributed to Conceptualization, Design, Simulation, Methodology, Experiment, and Writing – Original Draft. P.S. and J.C. contributed to Data Curation. M.Z., B.L., and G.X. contributed to Visualization and Writing – Reviewing and Editing. All authors reviewed and approved the final manuscript.

Acknowledgments

This work was supported by Shenzhen Natural Science Fund (the Stable Support Plan Program) (Grant No. GXWD20231129102419003).

References

1. Wokosin KA, Zoerb MC, Bertram TH, Kregel SJ (2026) A chemical ionization residual gas analyzer for the sensitive detection of atmospheric trace gases. J Am Soc Mass Spectrom 37(7):1623–1631
2. Albatayneh H, Younis MI (2025) A conductivity-based MEMS detector for helium. J Microelectromech Syst 34(5):645–652
3. Li P, Zhang F, Wang H, Yan H (2025) Hierarchically porous amino-functionalized microporous organic networks coated fiber for sensitive breath metabolite profiling: a noninvasive strategy for gastric cancer diagnosis. Anal Chem 97(50):27885–27893
4. Wang C, Mao Y, Lu H, Weng X, Dong F, Huang X (2026) High-performance Sb-doped SnO_2 nanoparticles sensor for fast detection of ppb-level HCHO as a lung cancer biomarker. Sens Actuat B-Chem 448:139022
5. Fendrych K, Porada R, Bas B (2025) A novel voltammetric strategy of furazidin determination with the use of co-ferrierite/mesoporous carbon modified glassy carbon electrode. J Electrochem Soc 172:017523
6. Huang W, Ding Q, Wang H, Wu Z, Luo Y, Shi W, Yang L, Liang Y, Liu C, Wu J (2023) Design of stretchable and self-powered sensing device for portable and remote trace biomarkers detection. Nat Commun 14:5221
7. Qian H, Chen L, Dai H, Chen F, Liu S, Du X, Gao S, Jiang Y, Li B, Zhu M, Xue G (2024) Glass-based micro-hotplate with low power consumption and TGV structure through anodic bonding and glass thermal reflow. J Microelectromech Syst 33(5):610–619
8. Gu L, Qian Y, Liu Y, Cheng M, Wei T, Liu Q, Wang R, Li W, Fu Z, Jiang H, Li Z, Liu B, Hu J (2026) Indium-doped $CuSnO_3$ perovskite hybrids for chemiresistive CO sensing. Chem Eng J 539:177250
9. Naricetti BMP, Ganesh GV, Thalluri LN, Daram NBB, Sankar CVR, Pandurangarao K, Guha K (2026) Development of a robust NO_2 gas sensor utilizing a micro heater and nano crystalline TiO_2 + WO_3 composite for enhanced sensing performance. Microsyst Technol 32:142
10. Kilic A, Alev O, Ziya OZ, Buyukkose S (2025) Fabrication and room temperature volatile organic compounds sensing performance of ZnO-based surface acoustic wave gas sensor. IEEE Sens J 25(23):42629–42637

11. Kumar R, Sharma D, Mandal N (2026) Synthesis of nano sensing film of stannic oxide and use of split IDT for SAW gas sensor for dichloromethane gas detection. IEEE Sens J 26(4):5595–5605
12. Qian H, Dai H, Zhu M, Jiang Y, Li B, Xue G (2025) Development of large-range rotary interferometer using a genetic algorithm for miniature FTIR spectrometer. In 2025 IEEE 38th International Conference on Micro Electro Mechanical Systems (IEEE MEMS) 728–731
13. Fard AM, Sarraf MJ, Khatib F, Kakhki EA (2025) High-sensitive hybrid non-circular photonic crystal fiber for H_2S detection. Microsyst Technol 31(9):2617–2623
14. Cavallaro A, Santonocito R, Pappalardo A, Tuccitto N, Sfrazzetto GT (2026) Methylamine gas sensing by optical array. Sens Actuat B-Chem 448:138936
15. Peng Y, Fei J, Qiu G, Dong H, Sun P, Xia H, Cai Y, Wang H, Wu B, Pang T, Zhang Z (2026) TDLAS-based distributed monitoring method for multi-component gas leakage in crude oil storage tanks. Opt Express 34(10):17934–17947
16. Yang L, Yuan H, Fang H, Gao Z, Ma R, Pan Y, Gao X, Niu M (2026) High sensitivity open seven-channel multipass cell TDLAS system for trace gas online monitoring. Sens Actuat B-Chem 454:139553
17. Zhang Q, Li D, Liu L, Wang Z, Zhang T, Sun G, Yu H, Wu M (2026) Miniaturized arched differential Helmholtz photoacoustic cell for trace gas detection. Sens Actuat A-Phys 408:118060
18. Chen P, Feng M, Liang M, Wang Q, Qiao Y, Jiao M, Li L, Shan C (2026) High-accuracy photoacoustic gas sensor enabled by deep learning-based concentration inversion from full waveforms. Photoacoustics 51:100868
19. Mu J, He Y, Qiao S, Sun H, Ma Y (2026) Photoacoustic spectroscopy sensing based on an annular quartz tuning fork. Sens Actuat B-Chem 463:140085
20. Zhang T, Wang W, Zhang Q, Wang J, Wei Y, Wang L, Gu Y, Li C (2025) A photoacoustic spectroscopy gas sensor based on double-cone resonant photoacoustic cells for simultaneous detection of CH_4/C_2H_2. Sens Actuat A-Phys 393:116819
21. Lang Z, Qiao S, Ma Y (2022) Acoustic microresonator based in-plane quartz-enhanced photoacoustic spectroscopy sensor with a line interaction mode. Opt Lett 47(6):1295
22. Sang C, Zhang C, Wang R, Qiao S, He Y, Ma Y (2025) Spherical acoustic resonator-based quartz-enhanced photoacoustic-photothermal dual spectroscopy sensing. Anal Chem 97(37):20536–20542
23. Yang B, Wang Y, Guo M, Li C, Zhao X, Qi H, Song J, Fan J, Gao Y, Fang Z, Chen K (2025) Ultrasensitive fiber-optic photoacoustic gas sensor based on miniaturized dual-enhancement spectrophone. IEEE Sens J 25(12):21464–21472
24. Yan C, Wang Q, Li T, Gao Z, Chen Y, Zhu Z, Li Z, Hou D, Liu Q (2025) Photoacoustic spectroscopy detection based on complementary interdigital cantilever enhanced Fabry-Perot acoustic sensor. Photoacoustics 46:100768

25. Trzpil W, Charensol J, Ayache D, Maurin N, Rousseau R, Vicet A, Bahriz M (2022) A silicon micromechanical resonator with capacitive transduction for enhanced photoacoustic spectroscopy. Sens Actuat B-Chem 353:131070
26. Yin Y, Ren D, Wang Y, Gao D, Shi J (2024) Design and test of a high-sensitivity MEMS capacitive resonator for photoacoustic gas detection. IEEE Sens J 24(24):40171–40178
27. Liu Y, Shi P, Chen Y, Lu Y, Zhu M, Li B, Xue G (2026) A MEMS skewed oscillating mirror with built-in piezoresistive sensor for photoacoustic gas detection. In 2026 IEEE 39th International Conference on Micro Electro Mechanical Systems (IEEE MEMS) 1056–1059
28. Xue G, Liu Y, Shi P, Wang M, Wang Q, Jiang Y, Li B, Zhu M (2026) A MEMS skewed oscillating mirror with piezoresistive transduction for photoacoustic CO_2 gas detection. J Microelectromech Syst 35(4):702–713
29. Jiang Y, Du M, Han X, Deng Z, Mao J, Chen L, Wang Y, Liu Y, Li Y, Wang R, Zheng C, Guo T (2026) Microcavity-enhanced optoelectronic fiber photoacoustic spectroscopy for ppb-level trace gas sensing. Light: Adv Manuf 7:28
30. Chen Y, Jiang L, Sun G, Li Y, Wang L, Wu D (2025) Dual-mode multi-microphone enhanced photoacoustic gas sensing system using a waveguide ring array. Anal Chem 97(46):25743–25751
31. Yang X, Li B, Geng X, Zhao T, Yu Q, Hou J, Zhang D, Liang Y, Xu K, Wu H, Yin X (2025) Ppb-level formaldehyde sensor utilizing a compact 3D-printed differential photoacoustic cell and a 320 nm UV laser. Photoacoustics 46:100780
32. Zhang C, Qiao S, He Y, Zhou S, Qi L, Ma Y (2023) Differential quartz-enhanced photoacoustic spectroscopy. Appl Phys Lett 122:241103

Figures

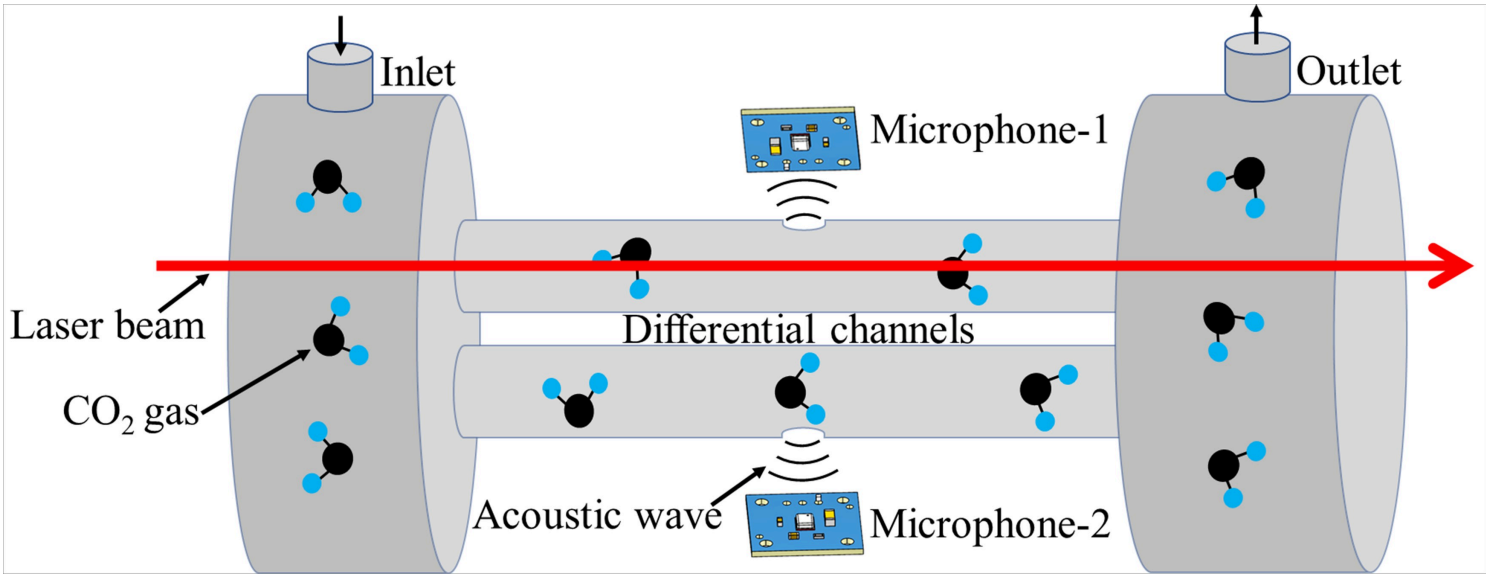


Figure 1

Schematic of the differential PAS gas measurement system.

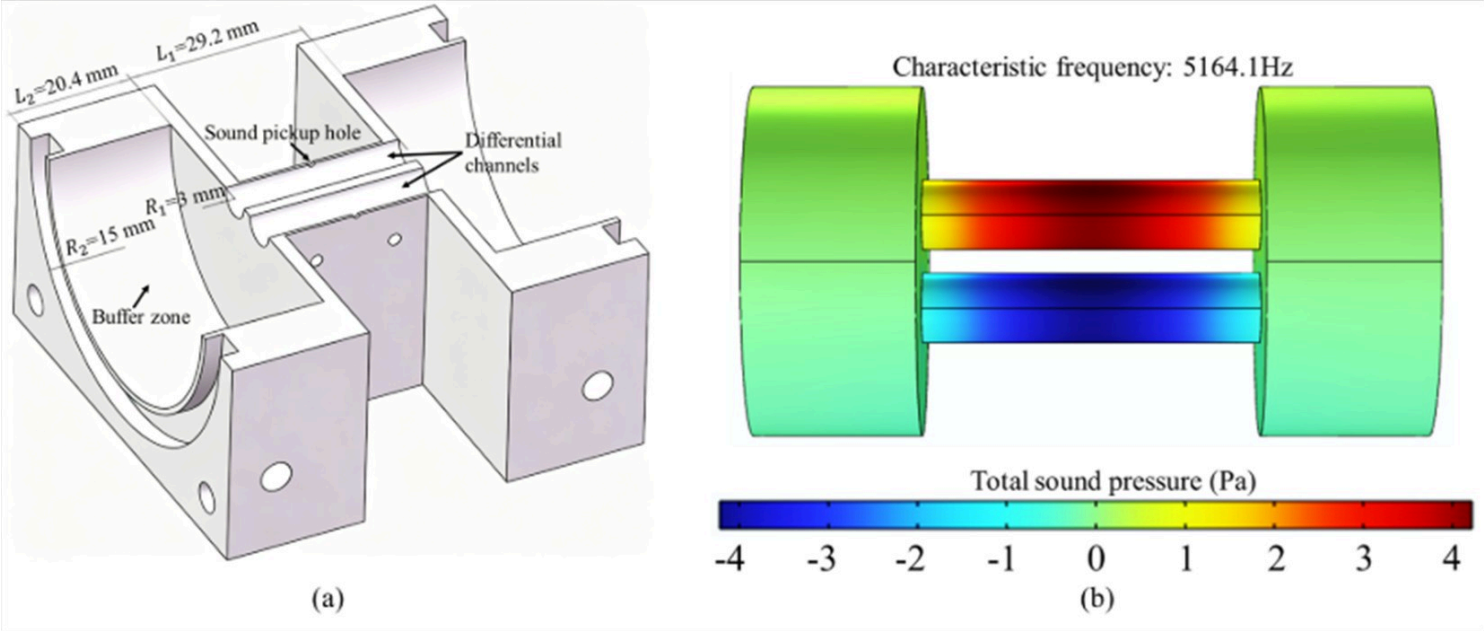


Figure 2

(a) Cross-section view of the designed differential PAC with the specific dimensions; (b) simulation of the acoustic pressure distribution of the differential PAC.

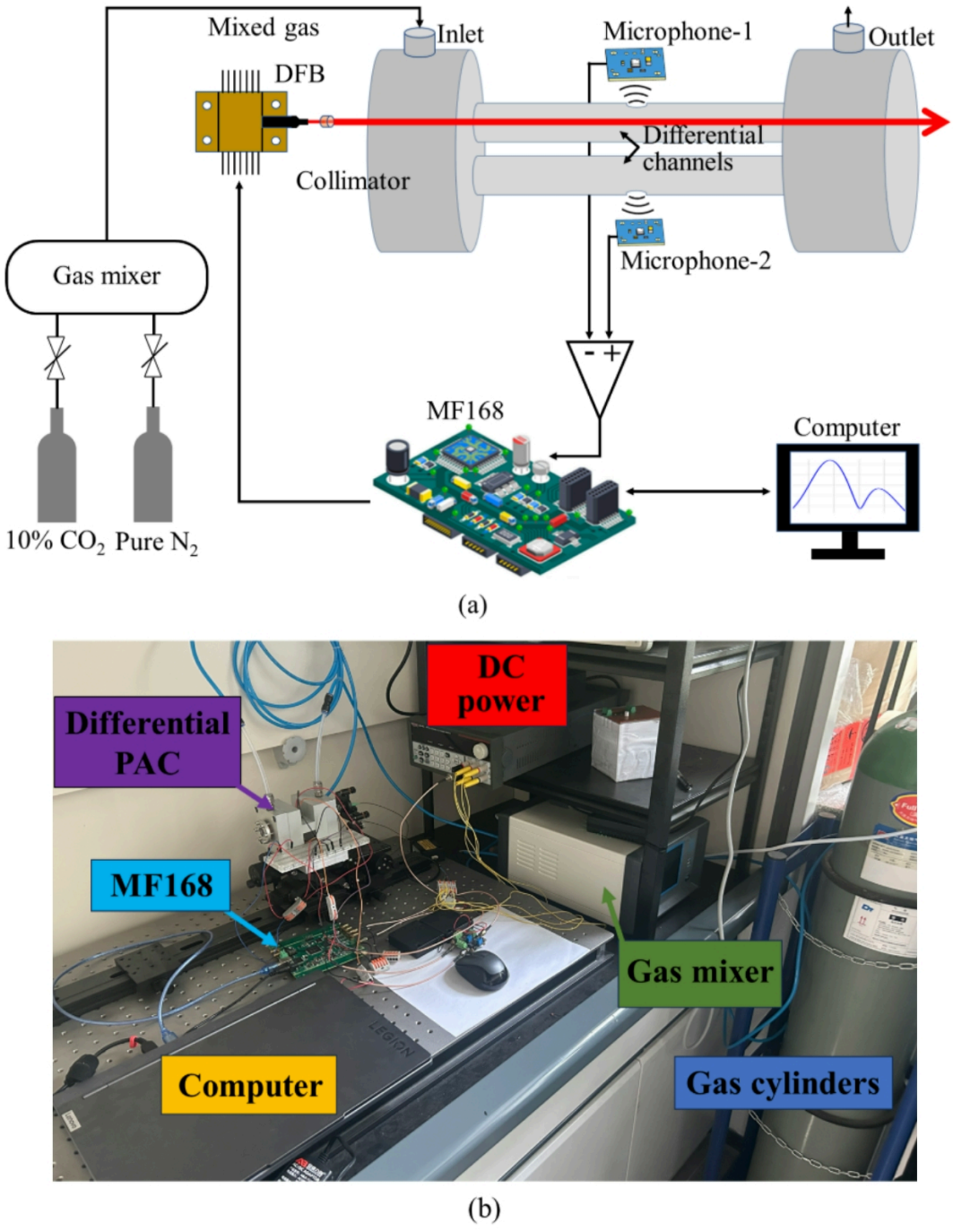


Figure 3

The differential PAS CO_2 measurement system: (a) schematic diagram; (b) actual setup.

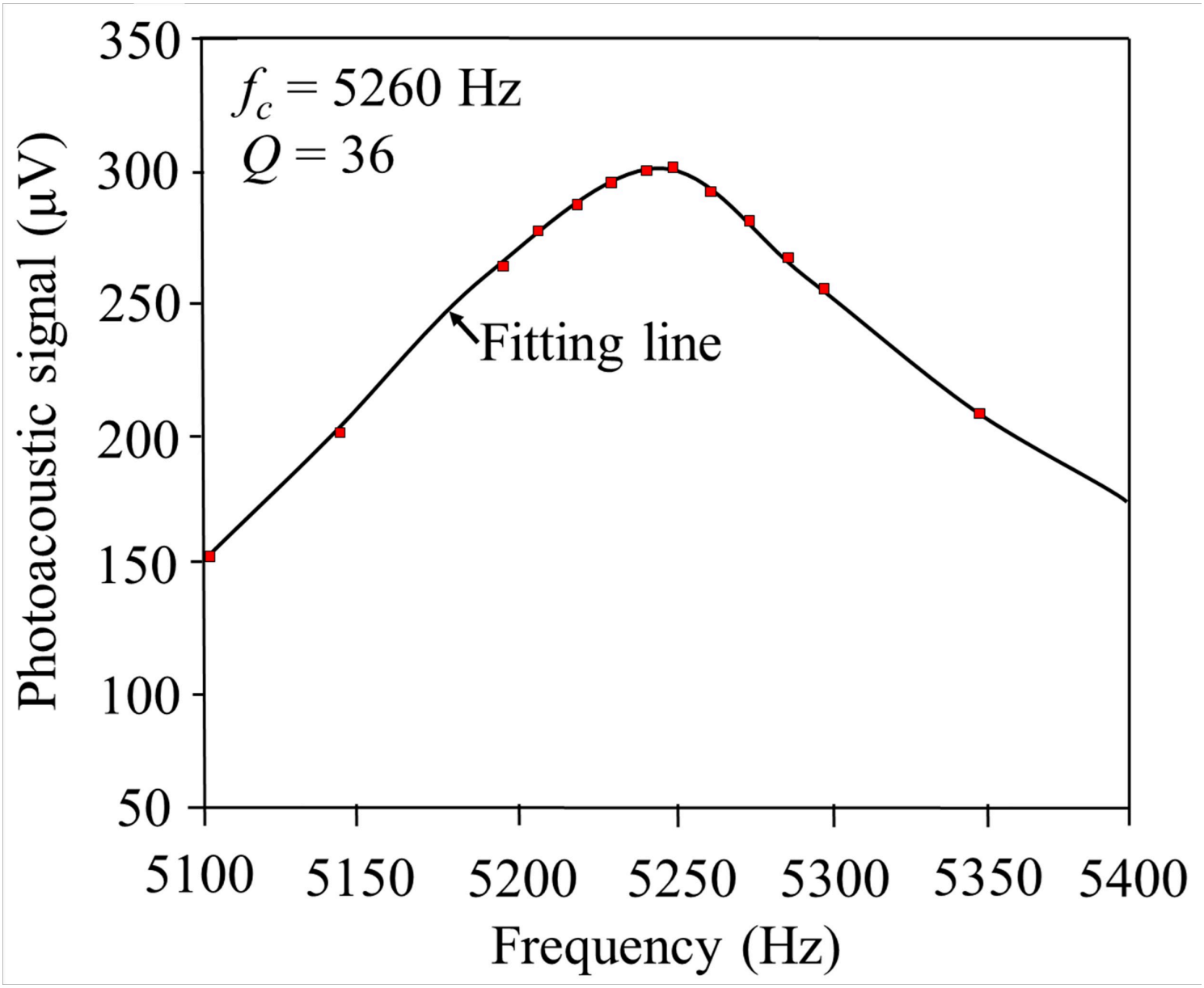


Figure 4

The frequency response of the fabricated differential PAC: the first-order resonant frequency at 5260 Hz with the *Q* factor of 36.

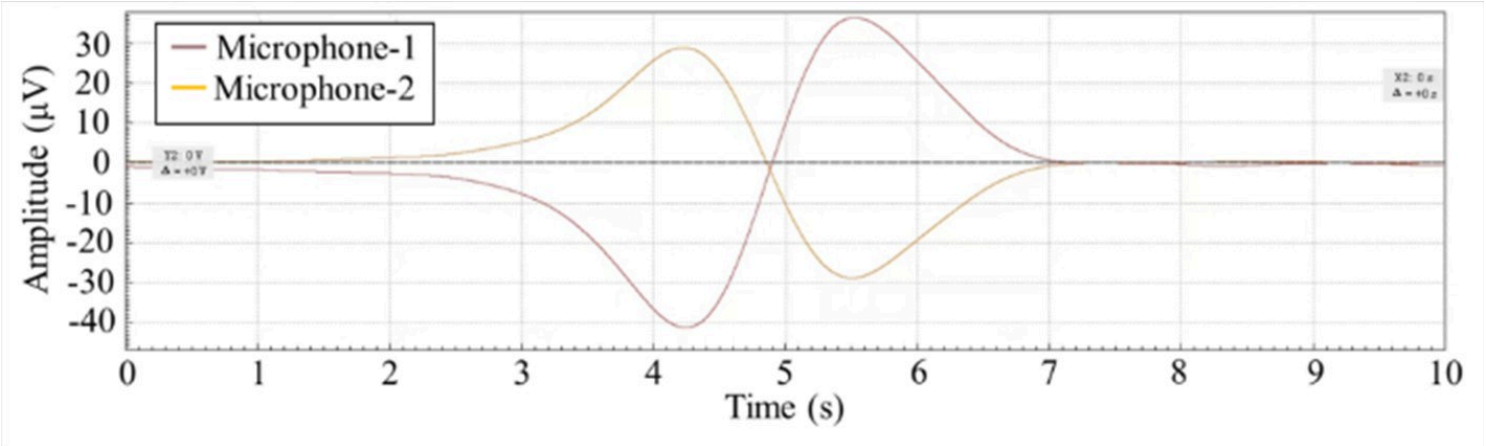


Figure 5

Differential 1*f* PA signal outputs from two microphones at a modulation period of 10 s with a certain CO_2 gas concentration.

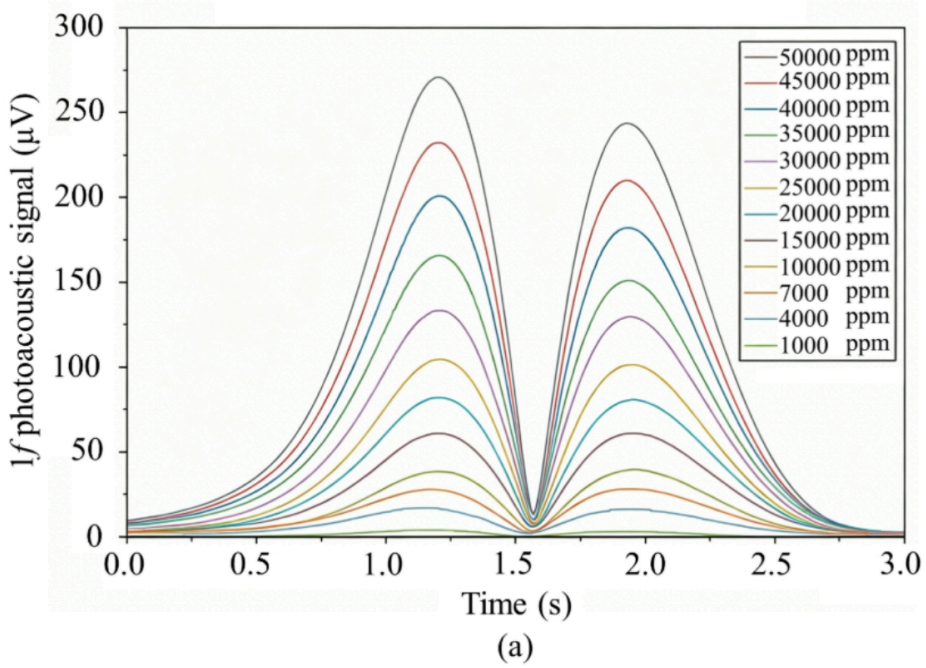


Figure 6

Differential PAC measurement results: (a) 1*f* PA signals at a modulation period of 4 s with a wide gas concentration range of from 1000 to 50000 ppm; (b) response relationship between 1*f* PA peak values and CO_2 gas concentrations (inset shows the amplified relationship in the low concentration range).

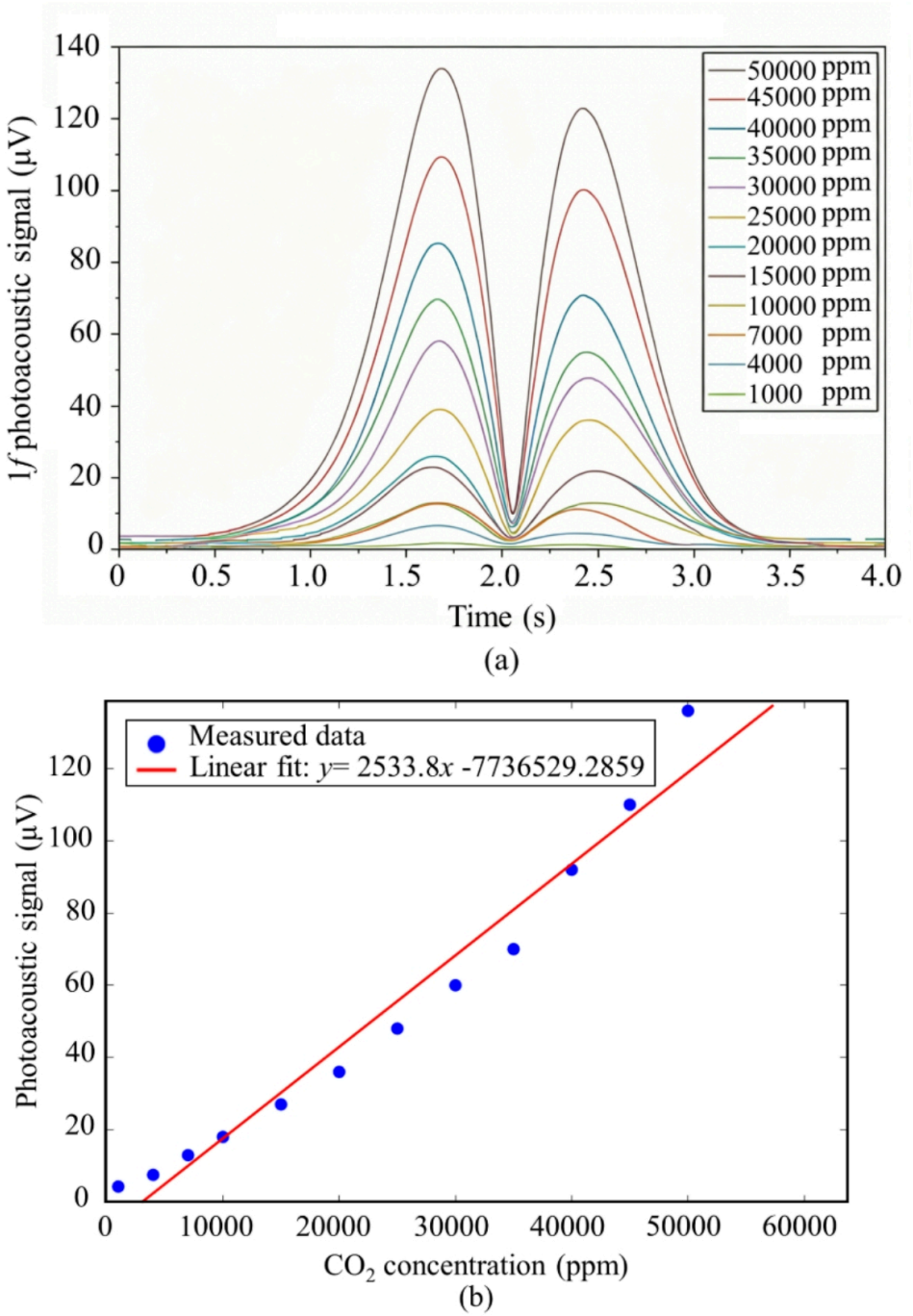


Figure 7

Single PAC measurement results: (a) 1*f* PA signals at a modulation period of 4 s with a wide gas concentration range of from 1000 to 50000 ppm; (b) response relationship between 1*f* PA peak values and CO_2 gas concentrations.

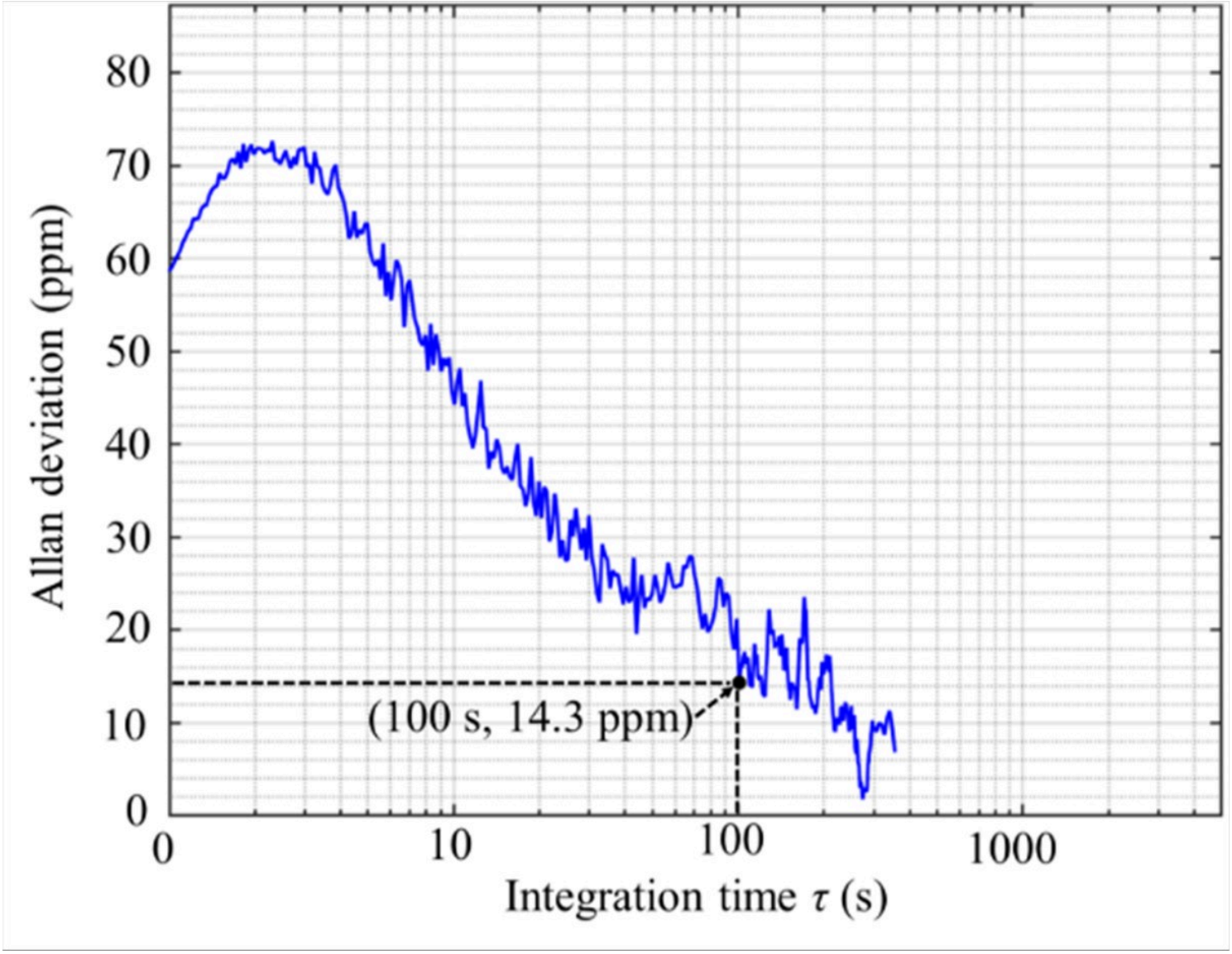


Figure 8

Allan-Werle deviation analysis of the differential PA measurement system with pure N_2 gas.